https://doi.org/10.5194/se-2020-144
Preprint. Discussion started: 26 August 2020

Solid Earth
Discussions
Open Access
EGU

Effect of normal stress on the friction of brucite: Application to slow earthquake in the mantle wedge

Hanaya Okuda[1,2], Ikuo Katayama[3], Hiroshi Sakuma[4], Kenji Kawai[1]

[1]Department of Earth and Planetary Science, School of Science, University of Tokyo, Bunkyo, 113-0033 Tokyo, Japan
[2]Department of Ocean Floor Geoscience, Atmosphere and Ocean Research Institute, University of Tokyo, Kashiwa, 277-8564 Chiba, Japan
[3]Department of Earth and Planetary Systems Science, Hiroshima University, Higashi-Hiroshima, 739-8526 Hiroshima, Japan
[4]Research Center for Functional Materials, National Institute for Materials Science, Tsukuba, 305-0044 Ibaraki, Japan

Correspondence to: Hanaya Okuda (okuda@aori.u-tokyo.ac.jp)

https://doi.org/10.5194/se-2020-144
Preprint. Discussion started: 26 August 2020

Solid Earth
Discussions
Open Access
EGU

Abstract

We report the results of friction experiments on brucite under both dry and water-saturated (wet) conditions under various normal stresses (10–60 MPa). The steady-state friction coefficients of brucite were determined to be 0.40 and 0.26 for the dry and wet cases, respectively, independent of the normal stress. Under dry conditions, velocity-weakening behavior was observed in all experiments at various normal stresses. Under wet conditions, velocity weakening was observed at low normal stress (10 and 20 MPa), whereas velocity strengthening was determined at a higher applied normal stress. ~~The m~~icrostructural observations on recovered experimental samples indicate localized deformation within ~~the~~ narrow shear band, implying that a small volume of brucite can control the bulk strength in an ultramafic setting and significantly change the frictional properties. Brucite is found to be the only mineral that has a low friction coefficient and exhibits unstable frictional behavior under hydrated mantle wedge conditions, explaining the occurrence of slow earthquakes in the mantle wedge.

https://doi.org/10.5194/se-2020-144
Preprint. Discussion started: 26 August 2020

1. Introduction

Serpentinite is generated by the hydration of ultramafic rocks and has various mineral compositions depending on temperature–pressure conditions of the MgO–SiO_2–H_2O system (Evans et al., 2013). As serpentinite has been observed in various important tectonic settings and is considered to contribute to the weakness of serpentinite-dominant areas, the frictional properties of serpentinite have been investigated for several decades (see Guillot et al., 2015; Hirth and Guillot, 2013 for a review). A large volume of serpentinite is located in the mantle wedge in which olivine-rich rock of the upper mantle is hydrated ~~due~~ by slab-derived water and its mechanical weakness could contribute to the aseismic behavior below the downdip limit of seismogenic zones (Hyndman and Peacock, 2003; Oleskevich et al., 1999).

The mantle wedge is mainly composed of an antigorite–olivine assemblage in the case of warm subduction zones like Cascadia, whereas a brucite–antigorite assemblage dominates in the case of cold subduction zones such as that in NE Japan (Peacock and Hyndman, 1999). Because fluids from subducting slabs have a high SiO_2 content, talc is stable in the vicinity of slab–mantle boundaries (Hirauchi et al., 2013; Peacock and Hyndman, 1999). The mineral composition of serpentinite has a strong effect on the mechanical behavior of bulk serpentinite because each serpentinite-related mineral, such as antigorite, brucite, and talc, has a different frictional behavior. Despite a variety of previous experimental investigations of the frictional properties of antigorite and talc (Hirauchi et al., 2013; Moore et al., 1997; Moore and Lockner, 2007, 2008; Okazaki and Katayama, 2015; Reinen et al., 1994; Sánchez-Roa et al., 2017; Takahashi et al., 2007; Tesei et al., 2018), brucite has rarely been considered in previous studies ~~compared with other serpentinite-related minerals~~, which might be due to the fact that it is difficult to detect brucite under natural conditions because of its fine-grained nature (Hostetler et al., 1966). Recent geological work on the paleo-mantle wedge in SW Japan revealed the presence of brucite and suggested that silica metamorphism has not widely occurred within the shallow mantle wedge (Kawahara et al., 2016; Mizukami et al., 2014). In addition, brucite was also detected in ultramafic clasts that erupted from mud volcanoes of

https://doi.org/10.5194/se-2020-144
Preprint. Discussion started: 26 August 2020


Solid Earth
Discussions
Open Access
EGU

the Mariana forearc mantle where the cold Mariana Plate subducts beneath the Philippine Sea Plate (D'Antonio and Kristensen, 2004). Because brucite is stable in the mantle wedge, its frictional properties should be investigated to understand the seismic activities in hydrated mantle wedges.

Only a few previous experimental studies have been conducted on the frictional properties of brucite. It was shown that brucite has friction coefficients of 0.40–0.46 (dry) or 0.28 (wet), which are lower than those of antigorite (Moore and Lockner, 2004, 2007; Morrow et al., 2000). Regarding the velocity dependence, ~~stick-slip behavior is significant~~, for dry brucite at both room and high temperature, implying velocity weakening. Conversely, wet brucite shows velocity-strengthening behavior at room temperature, which gradually changes to velocity weakening with increasing temperature (Moore et al., 2001; Moore and Lockner, 2007). Because the friction coefficient of ~~the~~ serpentinite gouge can be lowered by about ~10–15 % due to the presence of brucite (Moore et al., 2001) in addition to velocity-weakening behavior of brucite under certain conditions, the frictional characteristics of brucite might affect earthquake nucleation processes at mantle wedges. Although the mantle wedge is generally close to the downdip limit of seismogenic zones (Hyndman and Peacock, 2003; Oleskevich et al., 1999), many recent observations indicated slow earthquakes at the depth of the mantle wedge in various subduction zones (Audet and Kim, 2016; Obara and Kato, 2016). Therefore, the weak, unstable frictional behavior of brucite might be the key to understand the occurrence of slow earthquakes at mantle wedges.

The effective normal stress is an important parameter that constrains the frictional behavior because the apparent frictional strength of a material decreases with decreasing effective normal stress. Near lithostatic pore pressure conditions, which leads to low effective normal stress conditions, have been inferred based on seismic velocity structures at the plate interfaces of several subduction zones where slow earthquakes coincidentally occur such as Cascadia, SW Japan, Central Mexico, and Hikurangi (Audet et al., 2009; Audet and Kim, 2016; Eberhart-Phillips and Reyners, 2012; Matsubara et al., 2009; Shelly et al., 2006; Song and Kim, 2012). Importantly, low effective normal stress is favorable for the nucleation of slow

https://doi.org/10.5194/se-2020-144
Preprint. Discussion started: 26 August 2020


Solid Earth
Discussions
Open Access
EGU

earthquake (Liu and Rice, 2007, 2009; Rubin, 2008; Segall et al., 2010). Although the frictional behavior of brucite at low effective normal stress could be directly related to the occurrence of slow earthquake in the mantle wedge, previous studies have been conducted at high effective normal stresses of 100 or 150 MPa (Moore et al., 2001; Moore and Lockner, 2007) but not at low effective normal stress. In this study, we experimentally investigated the frictional behavior of brucite at various effective normal stresses ranging from 10 to 60 MPa to understand the effect of brucite on the seismic activities in hydrated mantle wedges. Because brucite shows a weak and unstable frictional behavior under a wide range of pressure–temperature conditions, it is a key material controlling the nucleation of earthquakes in hydrated mantle wedges.

2. Methods

2.1. Friction experiment

2.1.1. Sample preparation

Brucite nanoparticles with a grain size of 70 nm chemically synthesized by WAKO were used for the friction experiments to simulate its fine-grained nature (Fig. 1). The synthetic samples had a purity of 99.9 % (data from WAKO).

A biaxial testing machine at Hiroshima University, Japan, was used for all friction experiments in this study (Noda and Shimamoto, 2009). Two gouge layers were formed with three gabbro blocks (Fig. 1). The surfaces in contact with gouges were roughened before the experiments using Carborundum (grit 80) to prevent slip between the block and sample. All brucite samples were dried in the vacuum oven overnight under 120 °C before the experiments. This temperature was selected to remove adsorbed water and prevent the dehydroxylation of brucite into periclase (MgO). For the dry experiments, the brucite powder was quickly placed in each of the two gouges after removing it from the vacuum oven and blocks

https://doi.org/10.5194/se-2020-144
Preprint. Discussion started: 26 August 2020

Solid Earth
Discussions
Open Access
EGU

100 were put in the testing machine. For the wet experiments, dried brucite was mixed with distilled water until
101 saturation before placing it in the gouges and then sandwiched between blocks.
102
103 **2.1.2. Experimental procedures**
104 Normal stress was horizontally applied on the side blocks, and shear stress was applied vertically
105 by pushing the center block downward (Fig. 1). Before applying shear stress, the desired normal stress was
106 applied to the blocks for 1 h to prevent an effect of the compaction of the gouge during shear deformation
107 (nominally precompaction). For the wet experiments, the blocks and gouges were placed in the tank filled
108 with distilled water for 1 h under a normal stress of 250 kPa before the precompaction with the desired
109 normal stress such that water-saturated conditions were achieved. After the precompaction, shear stress was
110 applied with a constant load point velocity of 3 μm s^{-1}. Velocity step tests were repeatedly conducted after
111 the shear displacement reached 10 mm by abruptly increasing the load point velocity to 33 μm s^{-1} and
112 decreasing it to 3 μm s^{-1} after sliding of 1 mm (Fig. 2). The normal stress conditions of 10, 20, 40, and 60
113 MPa were tested for both the dry and wet cases to study the influence of effective normal stress. In addition,
114 several experiments were conducted with different shear displacements to investigate the evolution of the
115 gouge microstructure in both the dry and wet experiments (Table 1).
116

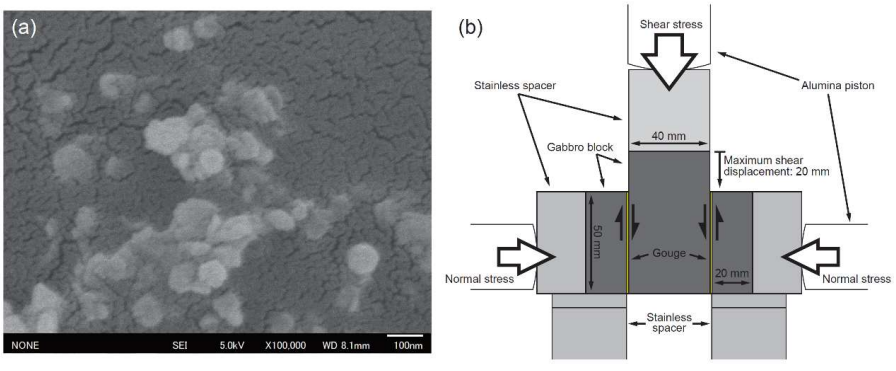

117

https://doi.org/10.5194/se-2020-144
Preprint. Discussion started: 26 August 2020

Figure 1: (a) SEM micrograph of synthetic brucite used in this study. The scale bar is 100 nm. (b) Schematic view of the biaxial testing machine used in this study.

2.2. Data analysis

2.2.1. Mechanical data

The friction coefficient μ was calculated from the ratio of the shear stress to the normal stress. Note that cohesion was not considered because the cohesion stresses were 0.36 and 0.47 MPa for the dry and wet cases, respectively, which are much smaller than the tested normal stress conditions. The shear displacement was corrected using the stiffness of the testing machine (4.4×10^8 N m^{-1}). The velocity step tests were analyzed using the rate- and state-dependent friction (RSF) law (Dieterich, 1979; Ruina, 1983). The slip dependency, which was calculated from the later part of each velocity step test with a shear displacement of 500 μm, was detrended before conducting the following analyses. Detrended data were fitted to the following the RSF law:

$$\mu = \mu_0 + a \ln\left(\frac{V}{V_0}\right) + b_1 \ln\left(\frac{V_0\theta_1}{d_{c1}}\right) + b_2 \ln\left(\frac{V_0\theta_2}{d_{c2}}\right), \quad (1)$$

where a, b_1 and b_2 are nondimensional parameters, μ_0 is the steady-state friction coefficient before the velocity step, V_0 and V are the sliding velocities before and after the velocity step, d_{c1} and d_{c2} are the characteristic slip distances, and θ_1 and θ_2 are the state variables. The transition of V was calculated by the following relationship:

$$\frac{d\mu}{dt} = k(V_{lp} - V), \quad (2)$$

where V_{lp} is the load point velocity, which was abruptly changed, and k is the system stiffness, which was treated as an unknown parameter (in μm^{-1}). The Dieterich (aging) law (Dieterich, 1979; Marone, 1998; Ruina, 1983) was used for the state variable in this study.

https://doi.org/10.5194/se-2020-144
Preprint. Discussion started: 26 August 2020

Solid Earth
Discussions
Open Access
EGU

$$\frac{d\theta_i}{dt} = 1 - \frac{V\theta_i}{d_{ci}}, i = 1, 2 \quad (3)$$

A MATLAB code, RSFit3000, developed to fit the velocity step and slide hold slide tests (Skarbek and Savage, 2019) was used for the analyses of velocity step tests. Second variables b_2, θ_2 and d_{c2} (Blanpied et al., 1998) were only introduced when the experimental data were poorly fitted (upsteps of HTB575 and HTB598; Fig. 4); otherwise, b_2 and θ_2 were treated as 0. The value of $a - b$ ($a - b_1 - b_2$, or $a - b_1$) was then calculated for each step, which describes the instability of the simulated fault: the state of fault is defined as velocity strengthening and stable when $a - b$ is positive, whereas it is defined as velocity weakening and potentially unstable when $a - b$ is negative. Note that d_c for the downsteps is larger than that for the upsteps. Because we chose to use the Dieterich (aging) law to fit the RSF law, d_c reflects the contact diameter of the asperity contact (Dieterich, 1979; Ruina, 1983). When the load point velocity is 3 μm s^{-1}, the lifetime of one asperity contact ~~becomes~~ longer than that with a load point velocity of 33 μm s^{-1}. Therefore, the contact diameter, d_c, for the load point velocity of 3 μm sec^{-1} (downsteps) ~~becomes~~ larger than that for 33 μm s^{-1} (upsteps). Although there are still debates on the choice of constitutive laws (Bhattacharya et al., 2015, 2017; Marone, 1998), the value of $a - b$ is more critical for seismic activities.

When the system is velocity weakening, that is, $a - b$ is negative, it starts to vibrate automatically (stick-slip) when the system stiffness is lower than ~~the~~ critical stiffness, whereas conditionally stable sliding is achieved when the system stiffness is higher than ~~the~~ critical stiffness. The critical stiffness k_c can be described as follows when quasi-static stick-slip behavior is assumed:

$$k_c = \frac{N(b - a)}{d_c}, \quad (4)$$

where N is the applied normal force (Ruina, 1983). Thus, as the normal force N applied to the velocity-weakening system increases, the system starts to show stick-slip behavior. In other words, the occurrence of stick-slip represents that the system is velocity-weakening.

https://doi.org/10.5194/se-2020-144
Preprint. Discussion started: 26 August 2020

Solid Earth Discussions

164 **2.2.2. Microstructure**

165 In the case of sheet-structure minerals, the friction between basal planes of the crystals [(0001)
166 plane for brucite] is thought to be significant due to their weak bonding. The shear surfaces of the samples
167 recovered from friction experiments using sheet-structure minerals often show smooth surfaces based on
168 platy particles aligned parallel to the sliding direction (Moore and Lockner, 2004). Under natural conditions,
169 the aligned platy particles of interconnected talc were reported to contribute to low friction coefficient of
170 ~~the~~ low angle normal fault (Collettini et al., 2009). The experimentally determined friction coefficients of
171 single-crystalline muscovite and chlorite are much smaller than those of powdered polycrystalline samples
172 (Horn and Deere, 1962; Kawai et al., 2015; Niemeijer, 2018; Okamoto et al., 2019).
173 Because these experiments indicate that the crystal orientation within the gouge has a significant
174 effect on the friction coefficients of sheet-structure minerals, observations of thin sections of recovered
175 samples were conducted after the experiments (Table 1) to investigate the effects of the deformation
176 structures and crystal orientation within the gouges on the frictional behaviors. Thin sections parallel to the
177 shear direction and normal to the gouges with a thickness of 30 μm were prepared. The scanning electron
178 microscope (SEM, JEOL JXA-8900 at the Atmosphere and Ocean Research Institute, University of Tokyo,
179 Japan) was used for the observation of the microstructures of the gouges. An accelerating voltage of 15 kV
180 and beam current of 10.0 nA were used for all backscattered electron (BSE) observations. The crystal
181 orientation was determined with a polarizing microscope at the University of Tokyo, Japan.
182

https://doi.org/10.5194/se-2020-144
Preprint. Discussion started: 26 August 2020

Solid Earth
Discussions
Open Access
EGU

3. Results

3.1. Mechanical behaviors

3.1.1. Friction coefficients

In general, both dry and wet experiments initially show high friction coefficients (hereafter peak friction coefficients) followed by slip-weakening trends ~~lasting about 10 mm shear displacement~~ toward ~~the~~ steady state (Figs. 2 and S1). The steady state friction coefficients at a shear displacement of ~20 mm for dry and wet conditions under all normal stress conditions were 0.40(4) and 0.26(3), respectively (Table 1). These steady-state friction coefficients are mostly independent of the applied normal stress (Fig. 3) and consistent with previous experimental results, that is, 0.38-0.46 and 0.28 for dry and wet brucite at an applied normal stress of 100 MPa at room temperature, respectively (Moore and Lockner, 2004, 2007). The friction coefficient for dry experiment is also close to the theoretical value of 0.30(3) (Okuda et al., 2019). Note that the peak friction coefficient of wet brucite at an effective normal stress of 60 MPa is high because of sudden stress drops in the initial stage of the shear displacement (Fig. S1).

https://doi.org/10.5194/se-2020-144
Preprint. Discussion started: 26 August 2020

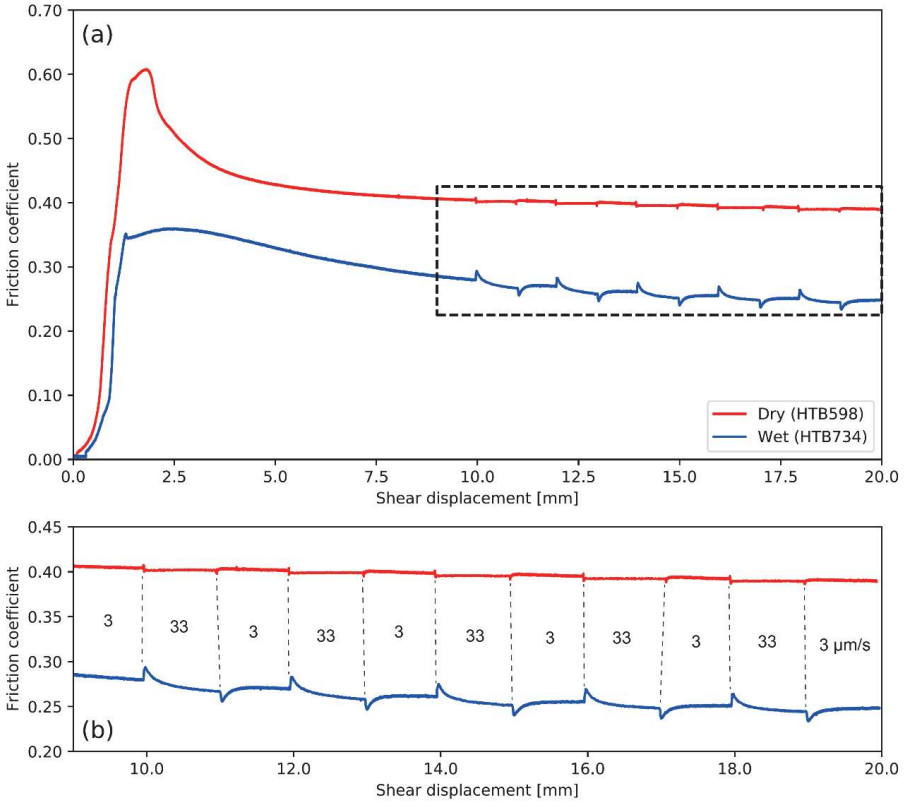

Figure 2: (a) Friction coefficients for dry (HTB598) and wet (HTB734) experiments at a normal stress of 20 MPa. Slip-weakening behavior was observed after the peak under both dry and wet conditions. (b) Enhanced view of velocity step sequences as indicated by the dotted square in (a). The velocities at given shear displacements are displayed between two lines.

https://doi.org/10.5194/se-2020-144
Preprint. Discussion started: 26 August 2020

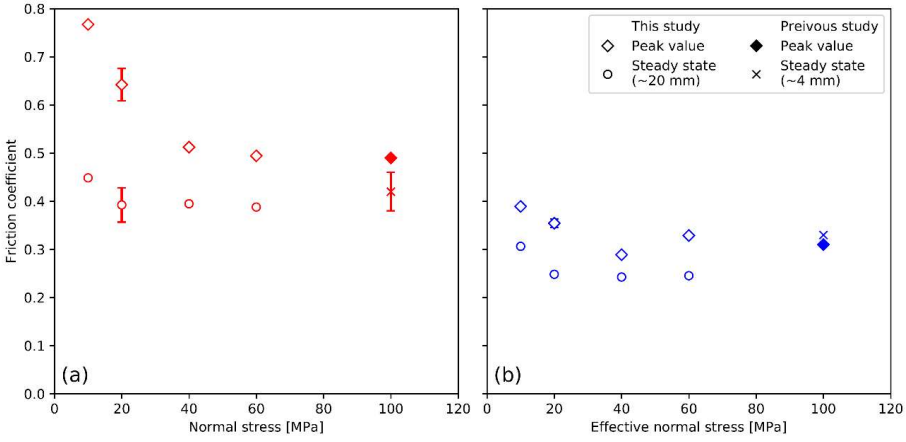

Figure 3: Relationship between normal stress and the peak or steady-state friction coefficients for the dry (a) and wet (b) experiments. Data at a normal stress of 100 MPa were obtained from previous experiments (Moore et al., 2001; Moore and Lockner, 2004, 2007; Morrow et al., 2000). The steady-state friction coefficients ~~insignificantly depend on~~ the applied normal stresses. For this study, the error bar represents the one-sigma standard deviation among multiple data. For 100 MPa dry data, the steady state value and the error bar denote the averaged value of stick-slip behavior and its amplitude, respectively. Note that the peak friction coefficient of wet brucite at an effective normal stress of 60 MPa is high because of sudden stress drops in the initial stage of the shear displacement (Fig. S1).

3.1.2. Velocity dependencies

For wet experiments, negative $a-b$ values were observed at low normal stresses of 10 and 20 MPa (Figs. 4a and b). However, the $a-b$ values became almost neutral at 40 MPa and positive at 60 MPa. A positive $a-b$ value was consistent with the previous experiments on wet brucite at an effective normal stress of 100 MPa (Moore et al., 2001; Moore and Lockner, 2007). The $a-b$ values obtained for the upsteps and downsteps insignificantly differ (Figs. 4a and b), which implies that the normal stress condition mainly controls the $a-b$ values. The constitutive parameter a insignificantly depends on the applied normal stress, whereas b decreases as the normal stress increases, leading to the transition from negative

https://doi.org/10.5194/se-2020-144
Preprint. Discussion started: 26 August 2020


Solid Earth
Discussions
Open Access
EGU

225 to positive $a-b$ values (Figs. 4e and f). The d_c values at different effective normal stresses
226 insignificantly differ (Figs. 4c and d).

227 For dry experiments, negative $a-b$ values were obtained at normal stresses of 10 and 20 MPa
228 (Figs. 4a and b). When the normal stress was higher than 40 MPa, stick-slip behavior was observed, which
229 implies a negative sign of $a-b$. This unstable stick-slip behavior was also observed in the case of the dry
230 experiment at a higher normal stress of 100 MPa (Moore and Lockner, 2004; Morrow et al., 2000). As
231 shown in the wet conditions, larger d_c values were observed for the downsteps (Figs. 4c and d). Although
232 the second variables b_2 and d_{c2} were introduced in certain experiments (HTB575 and HTB598), their
233 effects on the frictional characteristics are small because the b_2 values are much smaller than b_1 (Fig. 4e
234 and Table S1).

235 The constitutive parameters a and b and critical slip distance d_c of the dry and wet
236 experiments significantly differ. The a, b, and d_c values of the wet experiments are larger than those of
237 the dry experiments (Fig. 4). The critical slip distances d_c of the upsteps and downsteps under wet
238 conditions were 5–15 times and 3–4 times larger than those under dry conditions, respectively.
239
240

https://doi.org/10.5194/se-2020-144
Preprint. Discussion started: 26 August 2020

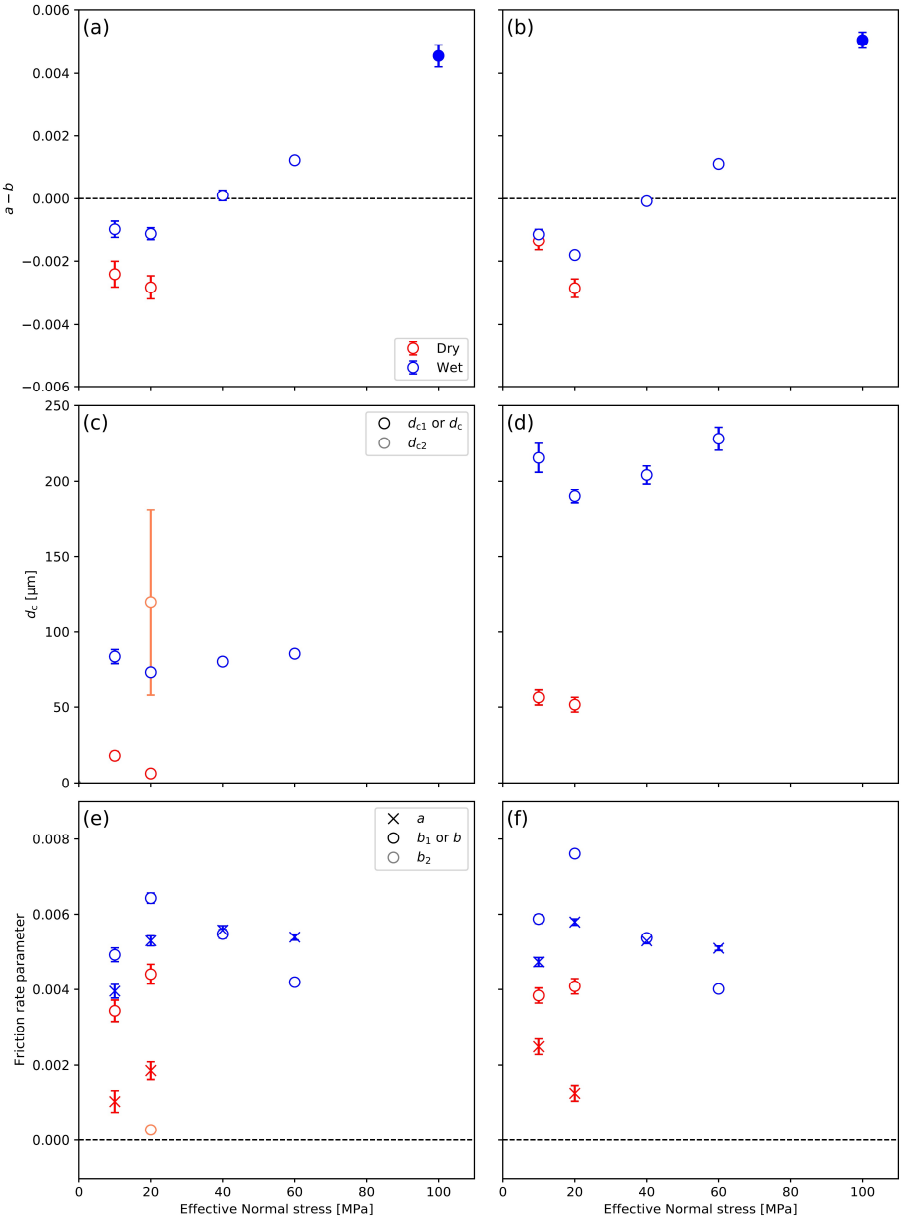

Figure 4: **Results of the velocity step tests. Values of $a - b$ for upsteps (a) and downsteps (b), d_c for upsteps (c) and for downsteps (d), a and b for upsteps (e) and for downsteps (f). The errors represent the one-sigma standard deviations of all upsteps or downsteps under each experimental condition including the errors of the nonlinear least square fitting processes. The $a - b$ values at a normal stress of 100 MPa were obtained from a**

https://doi.org/10.5194/se-2020-144
Preprint. Discussion started: 26 August 2020

previous study (solid symbol; Moore et al., 2001). Because stick-slip behavior was observed in the dry experiments at normal stresses of 40, 60, and 100 MPa, negative values of $a - b$ are expected; however, exact values could not be estimated (Sect. 3.1.2). Second variables b_2 and d_{c2} were introduced for upsteps of the dry experiments at a normal stress of 20 MPa.

3.2. Microstructure

3.2.1. Evolution of deformation structures

As all samples (both dry and wet) showed peak and steady states, we chose shear displacements before the peak friction coefficient (pre-yield), after the peak friction coefficient (post-yield), and in the steady state (10 mm). We followed the description of the microstructure of a sheared gouge by Logan et al. (1979). The results for the dry and wet experiments are shown in Figs. 5 and 6, respectively.

Before the shear loading, no shear structure was observed (Fig. 5a). When the shear force was loaded, the Riedel shear propagated in the pre-yield regime and the gouge ~~width shortened~~ rapidly at first (Figs. 5b and 6a). Subsequently, the boundary shear started to develop in the post-yield (Figs. 5c and 6b). In the steady state, the boundary shear was created by the gouge and the Riedel shear tilted subparallel to the boundary shear (Figs. 5d and 6c). The surfaces of the gabbro blocks were filled with brucite and the boundary shear was much smoother than the original block surface. These observations are consistent with those of previous studies (Haines et al., 2013; Logan et al., 1992; Marone, 1998), although clear Y shear and P foliation were not observed in this study. The gouge width remained almost constant following the post-yield and in the steady state. The width of the entire gouge in the steady state was 400 and 150 μm in the dry and wet cases, respectively (Figs. 5d and 6c). The narrow width of the gouge in the wet case may be the result of the leaking the sample during the experiment, although the deformation processes of the dry and wet cases do not differ, as shown above.

https://doi.org/10.5194/se-2020-144
Preprint. Discussion started: 26 August 2020

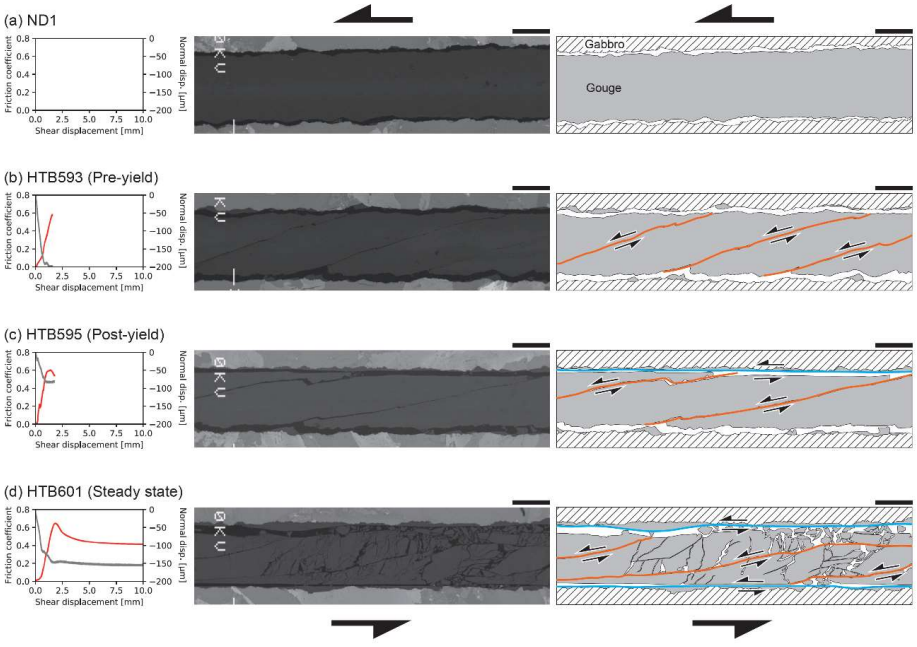

Figure 5: Backscattered electron (BSE) images showing the deformation of gouges (center) and corresponding interpretive sketches (right) of the dry experiments. The friction coefficients and normal displacement are shown in the left panels using colored and gray lines. The orange lines, blue lines, gray area, hatched area, and white area in the sketches correspond to the Riedel shear, boundary shear, brucite gouge, gabbro block, and epoxy resin, respectively. The arrows represent the slip directions. The scale bars represent 200 μm.

https://doi.org/10.5194/se-2020-144
Preprint. Discussion started: 26 August 2020

Solid Earth
Discussions
Open Access
EGU

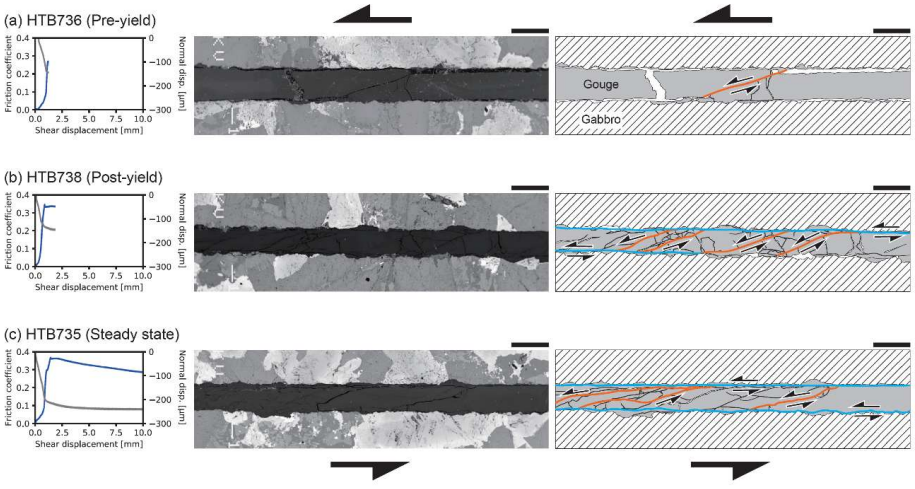

Figure 6: Backscattered electron (BSE) images showing the deformation of gouges (center) and corresponding interpretive sketches (right) of the wet experiments. See Fig. 6 for descriptions.

3.2.2. Crystal orientation

Because the elongation of brucite is length fast (Berman, 1932) and its birefringence is 0.014–0.020 (Deer et al., 2013), the interference color of brucite under crossed nicols with the sensitive color plate inserted becomes second-order blue or first-order yellow when the *c* axis of brucite is normal or parallel to the X′-direction of the sensitive color plate, respectively.

In the dry sample (HTB601; Figs. 7a and 7b), a second-order blue line can be observed parallel to the smooth boundary shear. This implies that the basal (0001) plane of the brucite particles is aligned along the boundary shear parallel to the shear direction. Based on the magnified view, the brucite particles are oriented within 10 μm around the boundary shear (Fig. 7b). Because the purple area indicates that the brucite particles are randomly oriented, the shear strain can be localized within a width of 10 μm. Hereafter, we call this oriented area “shear band.” In the wet samples, the crystals are also oriented along the boundary shear (Figs. 7c and 7d). The width of the shear band is 20 μm (Fig. 7d), that is, the same as in the dry case.

https://doi.org/10.5194/se-2020-144
Preprint. Discussion started: 26 August 2020

296 Note that detailed transmission electron microscopy is required in future studies to confirm the crystal
297 orientation and shear band width, similar to previous studies (Verberne et al., 2014a; Viti, 2011).

298

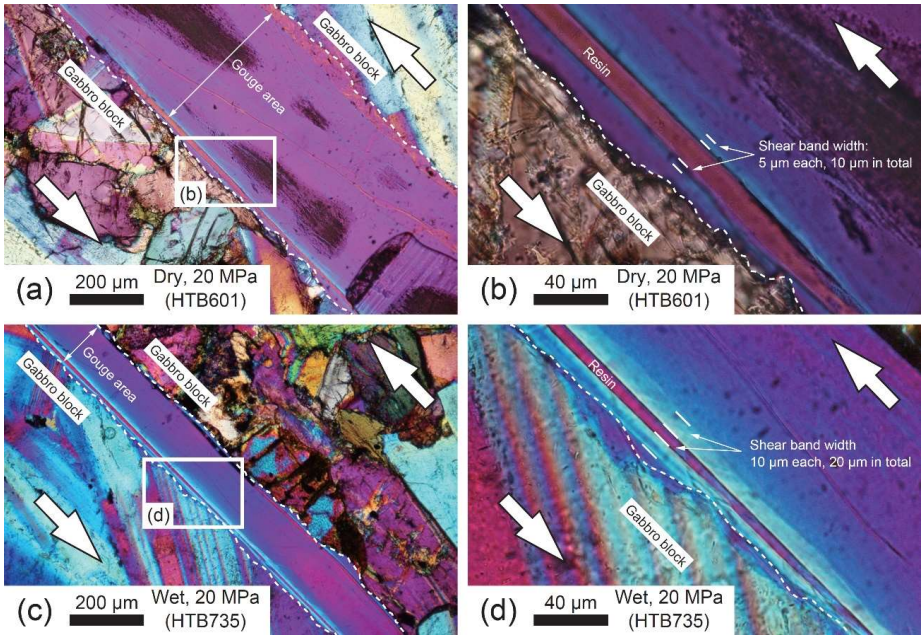

299

300 **Figure 7: Observation of the crystal orientation using the polarizing microscope under crossed nicols with the**
301 **sensitive color plate. The arrows indicate the shear direction. The X′-direction of the sensitive color plate is**
302 **parallel to the shear direction. (a) Dry experiment with 20 MPa normal stress (HTB601). (c) Wet experiment**
303 **with 20 MPa normal stress (HTB735). (b and d) Magnified views of (a) and (c), respectively. The shear band**
304 **widths are indicated in the figures. The white dashed line represents the boundary between the gabbro block**
305 **and brucite gouge.**

306

307

https://doi.org/10.5194/se-2020-144
Preprint. Discussion started: 26 August 2020

Solid Earth
Discussions
Open Access
EGU

4. Discussion

4.1. Mechanical weakness of a small amount of brucite

Based on the microstructural observations in Sect. 3.2, the boundary shear is smooth, filling the rough surface of the gabbro block as a "fault mirror" (Siman-Tov et al., 2013). The brucite particles are aligned along the boundary shear, ~~indicating~~ that the deformation within the narrow shear band is responsible for most of the deformation of the gouge during the steady state. In addition, the constant gouge thickness during the steady state suggests that the gouge deformation occurs parallel to the shear direction, ~~confirming that the shear deformation within the gouge occurs~~ within the shear band.

Because previous studies showed that friction with a smooth slip surface reduces the friction coefficients (Anthony and Marone, 2005), the smooth boundary shear observed in this study would reduce the friction coefficient with increasing shear displacement (Haines et al., 2013). In addition, the slip between the basal planes of sheet-structure minerals also plays an important role for weak friction because the friction between single crystals of sheet-structure minerals has a lower friction coefficient than that of powdered samples (Kawai et al., 2015; Niemeijer, 2018; Okamoto et al., 2019). Based on the observed alignment of the basal plane of brucite within the shear band, the friction between brucite crystals might enhance the weak friction of brucite. Because the preferred planes of nanoparticles tend to be aligned even when the velocity is low (Verberne et al., 2013, 2014b), nanoparticles could indirectly contribute to the slip-weakening behavior. Based on these phenomena, we conclude that the mechanical weakness of brucite observed in this study is derived from the smooth boundary shear of fine brucite particles and alignment of the basal plane of brucite parallel to the boundary shear.

The results of several previous experimental studies showed that the friction coefficient of a mixture of strong and weak materials inversely correlates with the volume of the weak materials (Giorgetti et al., 2015; Logan and Rauenzahn, 1987; Moore and Lockner, 2011; Niemeijer and Spiers, 2007; Shimamoto and Logan, 1981; Takahashi et al., 2007; Tembe et al., 2010). Based on the maximum amount

https://doi.org/10.5194/se-2020-144
Preprint. Discussion started: 26 August 2020

of brucite in serpentinite, that is ~20 vol. % (Kawahara et al., 2016; Moore et al., 2001), the expected friction coefficient of the antigorite–brucite mixture is 0.53, assuming a simple linear mixing law between the wet friction coefficients of 0.6 for antigorite and 0.26 for brucite. This value is not small, but the bulk friction coefficient of the mixture will decrease if weak brucite crystals are interconnected with each other. The microstructural observations showed that the shear band is less than 50 μm wide (Sect. 3.2.2; Fig. 7); therefore, a narrow network of brucite can ~~weaken~~ the bulk strength. The results of a recent petrographic study of a hydrated paleo-mantle wedge revealed brucite thin films parallel to antigorite particles, suggesting the significant role of brucite in the development of the sheared structure of the antigorite–brucite assemblage in the hydrated mantle wedge (Mizukami et al., 2014). Because the maximum width of the brucite film in the antigorite–brucite assemblage is several hundred micrometers (Kawahara et al., 2016; Mizukami et al., 2014), that is, larger than 50 μm, brucite has the potential to drastically weaken the bulk strength of serpentinite.

4.2. Application to the mantle wedge condition

To interpret the effect of brucite on the seismic activities in the mantle wedge, the effect of temperature should be considered because all our experiments were conducted under room-temperature conditions. According to previous experiments under hydrothermal conditions in which the temperature was varied, the friction coefficient the $a - b$ values decrease with increasing temperature (Moore et al., 2001; Moore and Lockner, 2007). Because a nearly neutral $a - b$ value was observed at an effective normal stress of 150 MPa and temperature of 340 °C (Moore et al., 2001), brucite shows ~~an~~ unstable behavior under a wide range of pressure–temperature conditions, especially at low effective normal stress. Based on the estimated frictional properties of brucite under the mantle wedge condition, we compared brucite to other mineral phases to interpret the earthquake processes within the mantle wedge (Fig. 8).

https://doi.org/10.5194/se-2020-144
Preprint. Discussion started: 26 August 2020


Solid Earth Discussions

In the mantle wedge, ultramafic minerals, such as olivine, transform into serpentine minerals, such as antigorite, talc, and brucite, due to hydration. In cold subduction zones, such as beneath NE Japan, likely containing brucite under the pressure–temperature conditions of the mantle wedge, the stable mineral assemblages are lizardite-brucite (Liz–Brc) at depths shallower than 50 km or antigorite–brucite (Atg–Brc) assemblage under deeper and warmer conditions (Peacock and Hyndman, 1999). Previous experimental studies on antigorite suggested potential seismic activities due to the unstable frictional behavior of antigorite at high temperatures above 450 °C (Okazaki and Katayama, 2015; Takahashi et al., 2011) at which crustal (granitic) rock shows stable friction (Fig. 8), whose friction coefficient (0.5–0.7) is not as low as that of brucite (Fig. 8). Although, lizardite, which destabilizes at ~200 °C, potentially shows ~~an~~ unstable behavior at low temperature (Moore et al., 1997), its friction coefficient is 0.4–0.5, which is lower than that of antigorite but higher than that of brucite (Fig. 8). Therefore, antigorite and lizardite are not preferably deformed if other weaker minerals, such as brucite, are present.

Another candidate of such a weak mineral stable under mantle wedge conditions is talc. Talc has a low friction coefficient of 0.1–0.2 at low to high temperatures (Fig. 8); therefore, it might contribute to the creep behavior of the San Andreas fault (Moore and Lockner, 2008) or weaken the slab–mantle interface (Hirauchi et al., 2013; Hyndman and Peacock, 2003). However, because talc has a stable frictional behavior at any temperature, leading to aseismic creep (Moore and Lockner, 2008; Sánchez-Roa et al., 2017), it cannot nucleate earthquakes. Considering the occurrence of talc in the mantle wedge, talc is stable at ~~when~~ high Si concentrations and temperature, whereas the mineral assemblage consists of brucite and antigorite when the Si content and temperature are low (Peacock and Hyndman, 1999). Talc was not widely observed in the paleo-mantle wedge exposed in the Shiraga body, central Shikoku, Japan, ~~with~~ the temperature–pressure condition where the antigorite–brucite system is stable (Kawahara et al., 2016; Mizukami et al., 2014). Although only antigorite stably exists in the antigorite–brucite stability field when the Si content is high, brucite is widely distributed in the Shiraga body (~10–15 %), suggesting low Si metasomatism in the

https://doi.org/10.5194/se-2020-144
Preprint. Discussion started: 26 August 2020


Solid Earth
Discussions
Open Access
EGU

379 shallow hydrated mantle wedge (Kawahara et al., 2016). Hence, brucite can stably exist within the mantle
380 wedge rather than talc. The distribution of brucite is associated with deformation and the brucite volume is
381 high enough to weaken the bulk strength as discussed in Sect. 4.1; therefore, brucite might be a key mineral
382 controlling the seismic activities in the shallow hydrated mantle wedge because brucite is the only mineral
383 that has weak, unstable frictional characteristics under a wide range of temperature–pressure conditions
384 (Fig. 8).

385 The results of recent seismological studies showed that ~~the~~ plate interfaces in the shallow mantle
386 wedge have a nearly lithostatic pore pressure due to slab-derived water at various subduction zones such as
387 SE Japan, Cascadia, Central Mexico, and Hikurangi (Audet et al., 2009; Audet and Kim, 2016; Eberhart-
388 Phillips and Reyners, 2012; Matsubara et al., 2009; Shelly et al., 2006; Song and Kim, 2012). Such low
389 effective normal stress conditions are conducive for brittle deformation rather than ductile behavior (French
390 and Condit, 2019; Gao and Wang, 2017). Slow earthquakes in the mantle wedge of various subduction
391 zones (Audet and Kim, 2016; Obara and Kato, 2016) might be induced by the low effective normal stress
392 because low effective normal stress conditions are conducive for the nucleation of slow earthquake (Liu
393 and Rice, 2007, 2009; Rubin, 2008; Segall et al., 2010). As $a - b$ value of brucite decreases with
394 decreasing effective normal stress, brucite at low effective normal stress possibly causes the nucleation of
395 slow earthquakes in the mantle wedge. Notably, the possible presence of talc or brucite-free antigorite due
396 to high Si content in the vicinity of the slab–mantle interface (Hirauchi et al., 2013; Peacock and Hyndman,
397 1999) might affect the partitioning of deformation (French and Condit, 2019) and the contribution of brucite
398 to the deformation. In addition, the linkage between high pore fluid pressure and the effective normal stress
399 is still debated (Hirth and Beeler, 2015; Noda and Takahashi, 2016); therefore, experiments under
400 hydrothermal conditions with high confining pressure and high pore fluid pressure must be conducted in
401 the future.
402

https://doi.org/10.5194/se-2020-144
Preprint. Discussion started: 26 August 2020

403

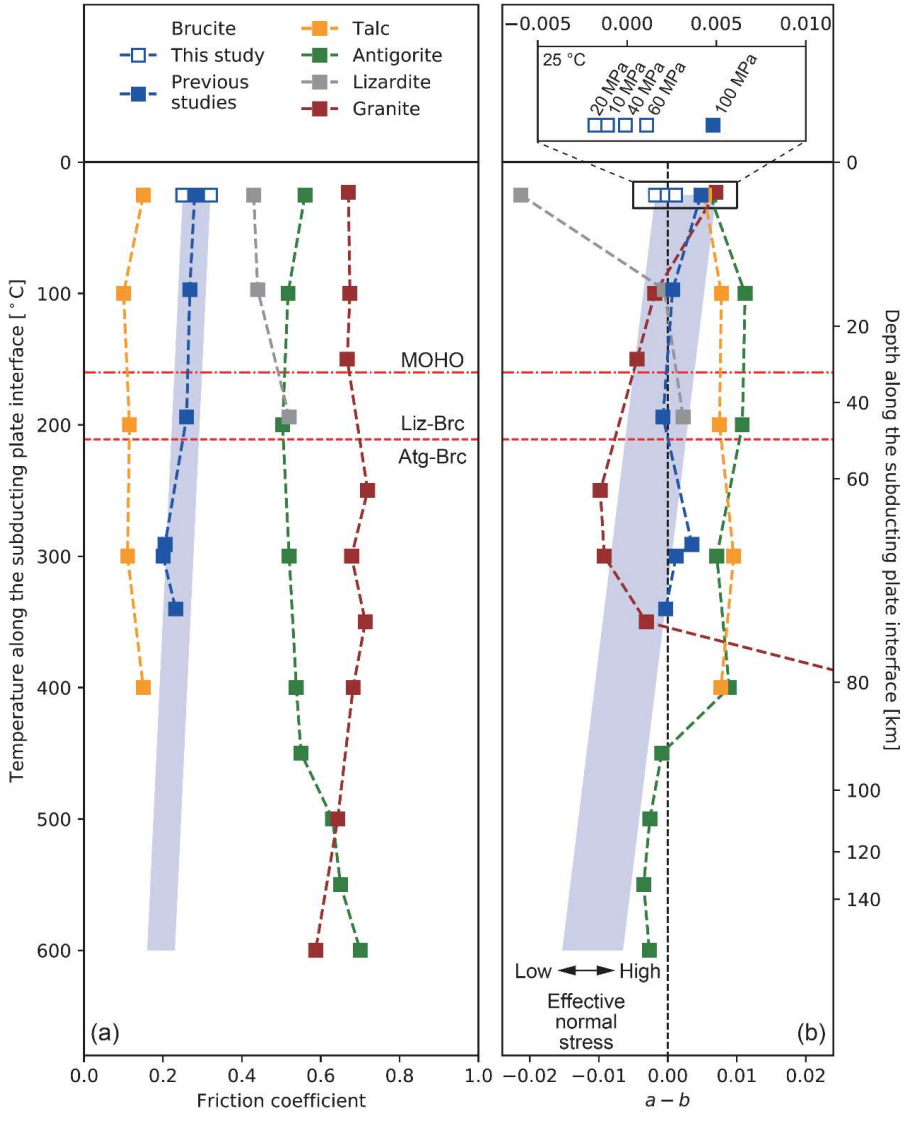

404

405 **Figure 8: Friction coefficients (a) and velocity dependences (b) of brucite (this study; Moore et al., 2001), talc**
406 **(Moore and Lockner, 2008), antigorite (Okazaki and Katayama, 2015; Takahashi et al., 2011), lizardite (Moore**
407 **et al., 1997), and granite (Blanpied et al., 1998). The vertical axes are identical to the temperature gradient along**
408 **the subduction interface in NE Japan (Peacock and Wang, 1999). The red chain horizontal line represents the**
409 **typical depth of the MOHO. The red dotted horizontal line represents the phase boundary between lizardite–**

https://doi.org/10.5194/se-2020-144
Preprint. Discussion started: 26 August 2020

410 **brucite (Liz–Brc) and antigorite–brucite (Atg–Brc; Peacock and Hyndman, 1999). The blue shaded areas are**
411 **the estimated frictional characteristics extrapolated from experimental results. With the decrease in the effective**
412 **normal stress, the $a - b$ value decreases, as indicated by the arrow. This trend was confirmed at room**
413 **temperature, as shown in the inset at the top of (b) and Fig. 4.**

414

415 **6. Conclusions**

416 In this study, the influence of effective normal stress on the frictional characteristics of brucite
417 was experimentally determined under both dry and water-saturated (wet) conditions at room temperature.
418 The steady-state friction coefficients of brucite are 0.40 and 0.26 in the dry and wet cases, respectively,
419 independently of the applied normal stress, while the peak friction coefficients are inversely correlated with
420 the applied normal stress. In all dry experiments, velocity-weakening or stick-slip behavior was observed
421 at every normal stress. In the wet experiments, velocity-weakening, -neutral, and -strengthening behaviors
422 were observed at normal stresses of 10 and 20, 40, and 60 MPa, respectively. Combining with the previously
423 reported temperature effect, this result suggests that brucite is weak and unstable under a wide temperature–
424 pressure condition. The microstructural observations reveal that the low friction coefficient and slip
425 weakening from the peak to steady-state friction coefficient are due to the smooth boundary shear and basal
426 plane orientation parallel to the boundary shear. Because the deformation is concentrated within a narrow
427 shear band with a width less than 50 μm, a small amount of brucite can weaken the bulk strength of the
428 antigorite–brucite assemblage. Compared to other serpentinite minerals, brucite is the only mineral that
429 shows both low friction coefficient and velocity-weakening behavior. Hence, we conclude that weak,
430 unstable brucite contributes to the nucleation of slow earthquake in the shallow hydrated mantle wedge.

431

432 **Table 1.** ***Summary of the experimental conditions and results.***

	Friction coefficient	$a - b$

https://doi.org/10.5194/se-2020-144
Preprint. Discussion started: 26 August 2020

Experiment	Condition	Normal stress	Final shear displacement	Peak value	Steady state (10 mm)	Steady state (20 mm)	Upsteps[a]	Downsteps[a]
HTB550	Dry	20 MPa	18 mm	0.67	0.36	0.35[b]	N/A	N/A
HTB575	Dry	20 MPa	20 mm	0.68	0.46	0.44	-0.0047(3)	-0.0048(2)
HTB580	Dry	10 MPa	20 mm	0.77	0.49	0.45	-0.0024(4)	-0.0014(3)
ND1	Dry	20 MPa	0 mm	N/A	N/A	N/A	N/A	N/A
HTB593	Dry	20 MPa	1.5 mm[c]	N/A	N/A	N/A	N/A	N/A
HTB595	Dry	20 MPa	2.0 mm[d]	0.60	N/A	N/A	N/A	N/A
HTB598	Dry	20 MPa	20 mm	0.61	0.41	0.39	-0.0010(2)	-0.0009(2)
HTB601	Dry	20 MPa	10 mm	0.65	0.42	N/A	N/A	N/A
HTB641	Dry	40 MPa	20 mm	0.51	0.41	0.395	Negative (Stick-slip)	Negative (Stick-slip)
HTB642	Dry	60 MPa	20 mm	0.50	0.40	0.39	Negative (Stick-slip)	Negative (Stick-slip)
HTB734	Wet	20 MPa	20 mm	0.35	0.28	0.25	-0.0011(2)	-0.0018(1)
HTB735	Wet	20 MPa	10 mm	0.37	0.29	N/A	N/A	N/A
HTB736	Wet	20 MPa	1.2 mm[c]	N/A	N/A	N/A	N/A	N/A

https://doi.org/10.5194/se-2020-144
Preprint. Discussion started: 26 August 2020


Solid Earth
Discussions
Open Access
EGU

HTB737	Wet	10 MPa	20 mm	0.39	0.32	0.31	-0.0010(3)	-0.0011(2)
HTB738	Wet	20 MPa	1.8 mm[d]	0.34	N/A	N/A	N/A	N/A
HTB739	Wet	40 MPa	20 mm	0.29	0.26	0.24	0.0001(2)	-0.0001(1)
HTB741	Wet	60 MPa	20 mm	0.33	0.25	0.25	0.0012(1)	0.0011(1)

Note. [a]All parameters (a, b, and d_c) used for the velocity step tests are listed in Table S1. [b]Value at the shear displacement of 18 mm. [c]Shear loading was stopped before the peak friction coefficient was reached. [d]Shear loading was stopped shortly after the peak friction coefficient was reached.

433

434

435

436 **Data availability**

437 The results of all experimental data are available in the Supporting Information.

438

439 **Author contributions**

440 H.O. conceptualized this study. H.O. and I.K. conducted the experiments. H.O. and H.S.
441 conducted analyses before experiments. H.O. carried out the formal analyses and microstructural analyses.
442 H.O. prepared the original manuscript, which was reviewed and edited by all coauthors. K.K. was the
443 supervisor. I.K., H.S., and K.K. designed the research project.

444

https://doi.org/10.5194/se-2020-144
Preprint. Discussion started: 26 August 2020

Competing interests

The authors declare that they have no conflict of interest.

Acknowledgement

We thank Y. Noda and R. Fujioka for the experiments, H. Ishisako for the preparation of thin sections, and A. Yamaguchi and N. Ogawa for SEM observations. This research was supported by KAKENHI grants (JP20J20413, JP20H00200, JP15H02147), and the Cooperative Program (No. 114, 2019) of the Atmosphere and Ocean Research Institute, University of Tokyo. H.O. is supported by JSPS and FMSP as a research fellow.

References

Anthony, J. L. and Marone, C.: Influence of particle characteristics on granular friction, J. Geophys. Res., 110, B08409, https://doi.org/10.1029/2004JB003399, 2005.

Audet, P. and Kim, Y.: Teleseismic constraints on the geological environment of deep episodic slow earthquakes in subduction zone forearcs: A review, Tectonophysics, 670, 1–15, https://doi.org/10.1016/j.tecto.2016.01.005, 2016.

Audet, P., Bostock, M. G., Christensen, N. I. and Peacock, S. M.: Seismic evidence for overpressured subducted oceanic crust and megathrust fault sealing, Nature, 457, 76–78, https://doi.org/10.1038/nature07650, 2009.

Berman, H.: Fibrous brucite from Quebec, Am. Mineral., 17, 313–316, 1932.

Bhattacharya, P., Rubin, A. M., Bayart, E., Savage, H. M. and Marone, C.: Critical evaluation of state evolution laws in rate and state friction: Fitting large velocity steps in simulated fault gouge with time-,

https://doi.org/10.5194/se-2020-144
Preprint. Discussion started: 26 August 2020

467 slip-, and stress-dependent constitutive laws, J. Geophys. Res. Solid Earth, 120, 6365–6385,
468 https://doi.org/10.1002/2015JB012437, 2015.
469 Bhattacharya, P., Rubin, A. M. and Beeler, N. M.: Does fault strengthening in laboratory rock friction
470 experiments really depend primarily upon time and not slip?, J. Geophys. Res. Solid Earth, 122, 6389–
471 6430, https://doi.org/10.1002/2017JB013936, 2017.
472 Blanpied, M. L., Marone, C. J., Lockner, D. A., Byerlee, J. D. and King, D. P.: Quantitative measure of
473 the variation in fault rheology due to fluid-rock interactions, J. Geophys. Res. Solid Earth, 103, 9691–
474 9712, https://doi.org/10.1029/98JB00162, 1998.
475 Collettini, C., Viti, C., Smith, S. A. F. and Holdsworth, R. E.: Development of interconnected talc
476 networks and weakening of continental low-angle normal faults, Geology, 37, 567–570,
477 https://doi.org/10.1130/G25645A.1, 2009.
478 D'Antonio, M. and Kristensen, M. B.: Serpentine and brucite of ultramafic clasts from the South
479 Chamorro Seamount (Ocean Drilling Program Leg 195, Site 1200): inferences for the serpentinization of
480 the Mariana forearc mantle, Mineral. Mag., 68, 887–904, https://doi.org/10.1180/0026461046860229,
481 2004.
482 Deer, W. A., Howie, R. A. and Zussman, J. (Eds.): An introduction to the rock-forming minerals, 3rd ed.,
483 Mineralogical Society, London, United Kingdom, 2013.
484 Dieterich, J. H.: Modeling of rock friction: 1. Experimental results and constitutive equations, J. Geophys.
485 Res., 84, 2161, https://doi.org/10.1029/JB084iB05p02161, 1979.
486 Eberhart-Phillips, D. and Reyners, M.: Imaging the Hikurangi Plate interface region, with improved local-
487 earthquake tomography, Geophys. J. Int., 190, 1221–1242, https://doi.org/10.1111/j.1365-
488 246X.2012.05553.x, 2012.
489 Evans, B. W., Hattori, K. and Baronnet, A.: Serpentinite: What, Why, Where?, Elements, 9, 99–106,
490 https://doi.org/10.2113/gselements.9.2.99, 2013.

https://doi.org/10.5194/se-2020-144
Preprint. Discussion started: 26 August 2020

491 French, M. E. and Condit, C. B.: Slip partitioning along an idealized subduction plate boundary at deep
492 slow slip conditions, Earth Planet. Sci. Lett., 528, 115828, https://doi.org/10.1016/j.epsl.2019.115828,
493 2019.
494 Gao, X. and Wang, K.: Rheological separation of the megathrust seismogenic zone and episodic tremor
495 and slip, Nature, 543, 416–419, https://doi.org/10.1038/nature21389, 2017.
496 Giorgetti, C., Carpenter, B. M. and Collettini, C.: Frictional behavior of talc-calcite mixtures, J. Geophys.
497 Res. Solid Earth, 120, 6614–6633, https://doi.org/10.1002/2015JB011970, 2015.
498 Guillot, S., Schwartz, S., Reynard, B., Agard, P. and Prigent, C.: Tectonic significance of serpentinites,
499 Tectonophysics, 646, 1–19, https://doi.org/10.1016/j.tecto.2015.01.020, 2015.
500 Haines, S. H., Kaproth, B., Marone, C., Saffer, D. M. and van der Pluijm, B. A.: Shear zones in clay-rich
501 fault gouge: A laboratory study of fabric development and evolution, J. Struct. Geol., 51, 206–225,
502 https://doi.org/10.1016/j.jsg.2013.01.002, 2013.
503 Hirauchi, K., den Hartog, S. A. M. and Spiers, C. J.: Weakening of the slab–mantle wedge interface
504 induced by metasomatic growth of talc, Geology, 41, 75–78, https://doi.org/10.1130/G33552.1, 2013.
505 Hirth, G. and Beeler, N. M.: The role of fluid pressure on frictional behavior at the base of the
506 seismogenic zone, Geology, 43, 223–226, https://doi.org/10.1130/G36361.1, 2015.
507 Hirth, G. and Guillot, S.: Rheology and tectonic significance of serpentinite, Elements, 9, 107–113,
508 https://doi.org/10.2113/gselements.9.2.107, 2013.
509 Horn, H. M. and Deere, D. U.: Frictional characteristics of minerals, Géotechnique, 12, 319–335,
510 https://doi.org/10.1680/geot.1962.12.4.319, 1962.
511 Hostetler, P. B., Coleman, R. G., Mumpton, F. A. and Evans, B. W.: Brucite in Alpine Serpentinites, Am.
512 Mineral., 51, 75–98, 1966.
513 Hyndman, R. D. and Peacock, S. M.: Serpentinization of the forearc mantle, Earth Planet. Sci. Lett., 212,
514 417–432, https://doi.org/10.1016/S0012-821X(03)00263-2, 2003.

https://doi.org/10.5194/se-2020-144
Preprint. Discussion started: 26 August 2020

515 Kawahara, H., Endo, S., Wallis, S. R., Nagaya, T., Mori, H. and Asahara, Y.: Brucite as an important
516 phase of the shallow mantle wedge: Evidence from the Shiraga unit of the Sanbagawa subduction zone,
517 SW Japan, Lithos, 254–255, 53–66, https://doi.org/10.1016/j.lithos.2016.02.022, 2016.
518 Kawai, K., Sakuma, H., Katayama, I. and Tamura, K.: Frictional characteristics of single and
519 polycrystalline muscovite and influence of fluid chemistry, J. Geophys. Res. Solid Earth, 120, 6209–
520 6218, https://doi.org/10.1002/2015JB012286, 2015.
521 Liu, Y. and Rice, J. R.: Spontaneous and triggered aseismic deformation transients in a subduction fault
522 model, J. Geophys. Res., 112, B09404, https://doi.org/10.1029/2007JB004930, 2007.
523 Liu, Y. and Rice, J. R.: Slow slip predictions based on granite and gabbro friction data compared to GPS
524 measurements in northern Cascadia, J. Geophys. Res. Solid Earth, 114, 1–19,
525 https://doi.org/10.1029/2008JB006142, 2009.
526 Logan, J. M. and Rauenzahn, K. A.: Frictional dependence of gouge mixtures of quartz and
527 montmorillonite on velocity, composition and fabric, Tectonophysics, 144, 87–108,
528 https://doi.org/10.1016/0040-1951(87)90010-2, 1987.
529 Logan, J. M., Dengo, C. A., Higgs, N. G. and Wang, Z. Z.: Fabrics of experimental fault zones: Their
530 development and relationship to mechanical behavior, in: Fault Mechanics and Transport Properties of
531 Rocks, edited by Evans, B, and Wong, T.F., Elsevier, 33–67, 1992.
532 Marone, C.: Laboratory-derived friction laws and their application to seismic faulting, Annu. Rev. Earth
533 Planet. Sci., 26, 643–696, https://doi.org/10.1146/annurev.earth.26.1.643, 1998.
534 Matsubara, M., Obara, K. and Kasahara, K.: High-VP/VS zone accompanying non-volcanic tremors and
535 slow-slip events beneath southwestern Japan, Tectonophysics, 472, 6–17,
536 https://doi.org/10.1016/j.tecto.2008.06.013, 2009.

https://doi.org/10.5194/se-2020-144
Preprint. Discussion started: 26 August 2020


Solid Earth
Discussions
Open Access
EGU

537 Mizukami, T., Yokoyama, H., Hiramatsu, Y., Arai, S., Kawahara, H., Nagaya, T. and Wallis, S. R.: Two
538 types of antigorite serpentinite controlling heterogeneous slow-slip behaviours of slab–mantle interface,
539 Earth. Planet. Scie. Lett., 401, 148–158, https://doi.org/10.1016/j.epsl.2014.06.009, 2014.
540 Moore, D. E. and Lockner, D. A.: Crystallographic controls on the frictional behavior of dry and water-
541 saturated sheet structure minerals, J. Geophys. Res., 109, B03401, https://doi.org/10.1029/2003JB002582,
542 2004.
543 Moore, D. E. and Lockner, D. A.: Comparative deformation behavior of minerals in serpentinized
544 ultramafic rock: Application to the slab-mantle interface in subduction zones, International Geology
545 Review, 49, 401–415, https://doi.org/10.2747/0020-6814.49.5.401, 2007.
546 Moore, D. E. and Lockner, D. A.: Talc friction in the temperature range 25°–400 °C: Relevance for fault-
547 zone weakening, Tectonophysics, 449, 120–132, https://doi.org/10.1016/j.tecto.2007.11.039, 2008.
548 Moore, D. E. and Lockner, D. A.: Frictional strengths of talc-serpentine and talc-quartz mixtures, J.
549 Geophys. Res., 116, B01403, https://doi.org/10.1029/2010JB007881, 2011.
550 Moore, D. E., Lockner, D. A., Ma, S., Summers, R. and Byerlee, J. D.: Strengths of serpentinite gouges at
551 elevated temperatures, J. Geophys. Res. Solid Earth, 102, 14787–14801,
552 https://doi.org/10.1029/97JB00995, 1997.
553 Moore, D. E., Lockner, D. A., Iwata, K., Tanaka, H. and Byerlee, J. D.: How brucite may affect the
554 frictional properties of serpentinite, USGS Open-File Report, 1–14, 2001.
555 Morrow, C. A., Moore, D. E. and Lockner, D. A.: The effect of mineral bond strength and adsorbed water
556 on fault gouge frictional strength, Geophys. Res. Lett., 27, 815–818,
557 https://doi.org/10.1029/1999GL008401, 2000.
558 Niemeijer, A. R.: Velocity-dependent slip weakening by the combined operation of pressure solution and
559 foliation development, Scientific Reports, 8, 4724, https://doi.org/10.1038/s41598-018-22889-3, 2018.

https://doi.org/10.5194/se-2020-144
Preprint. Discussion started: 26 August 2020

560 Niemeijer, A. R. and Spiers, C. J.: A microphysical model for strong velocity weakening in phyllosilicate-
561 bearing fault gouges, J. Geophys. Res., 112, B10405, https://doi.org/10.1029/2007JB005008, 2007.
562 Noda, H. and Shimamoto, T.: Constitutive properties of clayey fault gouge from the Hanaore fault zone,
563 southwest Japan, J. Geophys. Res., 114, B04409, https://doi.org/10.1029/2008JB005683, 2009.
564 Noda, H. and Takahashi, M.: The effective stress law at a brittle-plastic transition with a halite gouge
565 layer, Geophys. Res. Lett., 43, 1966–1972, https://doi.org/10.1002/2015GL067544, 2016.
566 Obara, K. and Kato, A.: Connecting slow earthquakes to huge earthquakes, Science, 353, 253–257,
567 https://doi.org/10.1126/science.aaf1512, 2016.
568 Okamoto, A. S., Verberne, B. A., Niemeijer, A. R., Takahashi, M., Shimizu, I., Ueda, T. and Spiers, C. J.:
569 Frictional properties of simulated chlorite gouge at hydrothermal conditions: Implications for subduction
570 megathrusts, J. Geophys. Res. Solid Earth, 124, 4545–4565, https://doi.org/10.1029/2018JB017205,
571 2019.
572 Okazaki, K. and Katayama, I.: Slow stick slip of antigorite serpentinite under hydrothermal conditions as
573 a possible mechanism for slow earthquakes, Geophys. Res. Lett., 42, 1099–1104,
574 https://doi.org/10.1002/2014GL062735, 2015.
575 Okuda, H., Kawai, K. and Sakuma, H.: First-principles investigation of frictional characteristics of
576 brucite: An application to its macroscopic frictional characteristics, J. Geophys. Res. Solid Earth, 124,
577 10423–10443, https://doi.org/10.1029/2019JB017740, 2019.
578 Oleskevich, D. A., Hyndman, R. D. and Wang, K.: The updip and downdip limits to great subduction
579 earthquakes: Thermal and structural models of Cascadia, south Alaska, SW Japan, and Chile, J. Geophys.
580 Res. Solid Earth, 104, 14965–14991, https://doi.org/10.1029/1999JB900060, 1999.
581 Peacock, S. M. and Hyndman, R. D.: Hydrous minerals in the mantle wedge and the maximum depth of
582 subduction thrust earthquakes, Geophys. Res. Lett., 26, 2517–2520,
583 https://doi.org/10.1029/1999GL900558, 1999.

https://doi.org/10.5194/se-2020-144
Preprint. Discussion started: 26 August 2020

584 Peacock, S. M. and Wang, K.: Seismic consequences of warm versus cool subduction metamorphism:
585 Examples from southwest and northeast Japan, Science, 286, 937–939,
586 https://doi.org/10.1126/science.286.5441.937, 1999.
587 Reinen, L. A., Weeks, J. D. and Tullis, T. E.: The frictional behavior of lizardite and antigorite
588 serpentinites: Experiments, constitutive models, and implications for natural faults, Pure Appl. Geophys.,
589 143, 317–358, https://doi.org/10.1007/BF00874334, 1994.
590 Rubin, A. M.: Episodic slow slip events and rate-and-state friction, J. Geophys. Res., 113, B11414,
591 https://doi.org/10.1029/2008JB005642, 2008.
592 Ruina, A. L.: Slip instability and state variable friction laws, J. Geophys. Res. Solid Earth, 88, 10359–
593 10370, https://doi.org/10.1029/JB088iB12p10359, 1983.
594 Sánchez-Roa, C., Faulkner, D. R., Boulton, C., Jimenez-Millan, J. and Nieto, F.: How phyllosilicate
595 mineral structure affects fault strength in Mg-rich fault systems, Geophys. Res. Lett., 44, 5457–5467,
596 https://doi.org/10.1002/2017GL073055, 2017.
597 Segall, P., Rubin, A. M., Bradley, A. M. and Rice, J. R.: Dilatant strengthening as a mechanism for slow
598 slip events, J. Geophys. Res., 115, B12305, https://doi.org/10.1029/2010JB007449, 2010.
599 Shelly, D. R., Beroza, G. C., Ide, S. and Nakamula, S.: Low-frequency earthquakes in Shikoku, Japan,
600 and their relationship to episodic tremor and slip, Nature, 442, 188–191,
601 https://doi.org/10.1038/nature04931, 2006.
602 Shimamoto, T. and Logan, J. M.: Effects of simulated clay gouges on the sliding behavior of Tennessee
603 sandstone, Tectonophysics, 75, 243–255, https://doi.org/10.1016/0040-1951(81)90276-6, 1981.
604 Siman-Tov, S., Aharonov, E., Sagy, A. and Emmanuel, S.: Nanograins form carbonate fault mirrors,
605 Geology, 41, 703–706, https://doi.org/10.1130/G34087.1, 2013.

https://doi.org/10.5194/se-2020-144
Preprint. Discussion started: 26 August 2020

606 Skarbek, R. M. and Savage, H. M.: RSFit3000: A MATLAB GUI-based program for determining rate
607 and state frictional parameters from experimental data, Geosphere, 15, 1665–1676,
608 https://doi.org/10.1130/GES02122.1, 2019.
609 Song, T.-R. A. and Kim, Y.: Localized seismic anisotropy associated with long-term slow-slip events
610 beneath southern Mexico, Geophys. Res. Lett., 39, L09308, https://doi.org/10.1029/2012GL051324,
611 2012.
612 Takahashi, M., Mizoguchi, K., Kitamura, K. and Masuda, K.: Effects of clay content on the frictional
613 strength and fluid transport property of faults, J. Geophys. Res., 112, B08206,
614 https://doi.org/10.1029/2006JB004678, 2007.
615 Takahashi, M., Uehara, S.-I., Mizoguchi, K., Shimizu, I., Okazaki, K. and Masuda, K.: On the transient
616 response of serpentine (antigorite) gouge to stepwise changes in slip velocity under high-temperature
617 conditions, J. Geophys. Res., 116, B10405, https://doi.org/10.1029/2010JB008062, 2011.
618 Tembe, S., Lockner, D. A. and Wong, T.-F.: Effect of clay content and mineralogy on frictional sliding
619 behavior of simulated gouges: Binary and ternary mixtures of quartz, illite, and montmorillonite, J.
620 Geophys. Res., 115, B03416, https://doi.org/10.1029/2009JB006383, 2010.
621 Tesei, T., Harbord, C. W. A., De Paola, N., Collettini, C. and Viti, C.: Friction of mineralogically
622 controlled serpentinites and implications for fault weakness, J. Geophys. Res. Solid Earth, 123, 6976–
623 6991, https://doi.org/10.1029/2018JB016058, 2018.
624 Verberne, B. A., De Bresser, J. H. P., Niemeijer, A. R., Spiers, C. J., de Winter, D. A. M. and Plümper,
625 O.: Nanocrystalline slip zones in calcite fault gouge show intense crystallographic preferred orientation:
626 Crystal plasticity at sub-seismic slip rates at 18–150 °C, Geology, 41, 863–866,
627 https://doi.org/10.1130/G34279.1, 2013.

https://doi.org/10.5194/se-2020-144
Preprint. Discussion started: 26 August 2020

628 Verberne, B. A., Spiers, C. J., Niemeijer, A. R., De Bresser, J. H. P., de Winter, D. A. M. and Plümper,
629 O.: Frictional properties and microstructure of calcite-rich fault gouges sheared at sub-seismic sliding
630 velocities, Pure Appl. Geophys., 171, 2617–2640, https://doi.org/10.1007/s00024-013-0760-0, 2014a.
631 Verberne, B. A., Plümper, O., de Winter, D. A. M. and Spiers, C. J.: Superplastic nanofibrous slip zones
632 control seismogenic fault friction, Science, 346, 1342–1344, https://doi.org/10.1126/science.1259003,
633 2014b.
634 Viti, C.: Exploring fault rocks at the nanoscale, J. Struct. Geol., 33, 1715–1727,
635 https://doi.org/10.1016/j.jsg.2011.10.005, 2011.
636